Delft University of Technology

Additively manufactured and surface biofunctionalized porous nitinol

Gorgin Karaji, Zahra; Speirs, M.; Dadbakhsh, S.; Kruth, JP; Weinans, Harrie; Zadpoor, Amir; Amin Yavari, Saber

DOI
10.1021/acsami.6b14026

Publication date
2017

Document Version
Final published version

Published in
ACS Applied Materials and Interfaces

Citation (APA)
Gorgin Karaji, Z., Speirs, M., Dadbakhsh, S., Kruth, JP., Weinans, H., Zadpoor, A., & Amin Yavari, S. (2017). Additively manufactured and surface biofunctionalized porous nitinol. *ACS Applied Materials and Interfaces*, *9*(2), 1293-1304. https://doi.org/10.1021/acsami.6b14026

Important note
To cite this publication, please use the final published version (if applicable).
Please check the document version above.

Copyright
Other than for strictly personal use, it is not permitted to download, forward or distribute the text or part of it, without the consent of the author(s) and/or copyright holder(s), unless the work is under an open content license such as Creative Commons.

Takedown policy
Please contact us and provide details if you believe this document breaches copyrights.
We will remove access to the work immediately and investigate your claim.

This work is downloaded from Delft University of Technology.
For technical reasons the number of authors shown on this cover page is limited to a maximum of 10.

ACS APPLIED MATERIALS & INTERFACES

Research Article

www.acsami.org

Additively Manufactured and Surface Biofunctionalized Porous Nitinol

Z. Gorgin Karaji,[†,§] M. Speirs,[⊥] S. Dadbakhsh,[⊥] J.-P. Kruth,[⊥] H. Weinans,[†,¶,‡] A. A. Zadpoor,[¶] and S. Amin Yavari*[,†,¶]

[†]Department of Orthopedics and [‡]Department of Rheumatology, University Medical Centre Utrecht, 3584 CX Utrecht, The Netherlands

[§]Department of Mechanical Engineering, Kermanshah University of Technology, 63766-67178 Kermanshah, Iran

[⊥]PMA Division, Department of Mechanical Engineering, KU Leuven, 3001 Leuven, Belgium

[¶]Department of Biomechanical Engineering, Delft University of Technology, 2628 CD Delft, The Netherlands

Downloaded via TU DELFT on December 15, 2020 at 09:23:36 (UTC).
See https://pubs.acs.org/sharingguidelines for options on how to legitimately share published articles.

ABSTRACT: Enhanced bone tissue regeneration and improved osseointegration are among the most important goals in design of multifunctional orthopedic biomaterials. In this study, we used additive manufacturing (selective laser melting) to develop multifunctional porous nitinol that combines superelasticity with a rationally designed microarchitecture and biofunctionalized surface. The rational design based on triply periodic minimal surfaces aimed to properly adjust the pore size, increase the surface area (thereby amplifying the effects of surface biofunctionalization), and resemble the curvature characteristics of trabecular bone. The surface of additively manufactured (AM) porous nitinol was biofunctionalized using polydopamine-immobilized rhBMP2 for better control of the release kinetics. The actual morphological properties of porous nitinol measured by microcomputed tomography (e.g., open/close porosity, and surface area) closely matched the design values. The superelasticity originated from the austenite phase formed in the nitinol porous structure at room temperature. Polydopamine and rhBMP2 signature peaks were confirmed by X-ray photoelectron spectroscopy and Fourier transform infrared spectroscopy tests. The release of rhBMP2 continued until 28 days. The early time and long-term release profiles were found to be adjustable independent of each other. In vitro cell culture showed improved cell attachment, cell proliferation, cell morphology (spreading, spindle-like shape), and cell coverage as well as elevated levels of ALP activity and increased calcium content for biofunctionalized surfaces as compared to as-manufactured specimens. The demonstrated functionalities of porous nitinol could be used as a basis for deployable orthopedic implants with rationally designed microarchitectures that maximize bone tissue regeneration performance by release of biomolecules with adjustable and well-controlled release profiles.

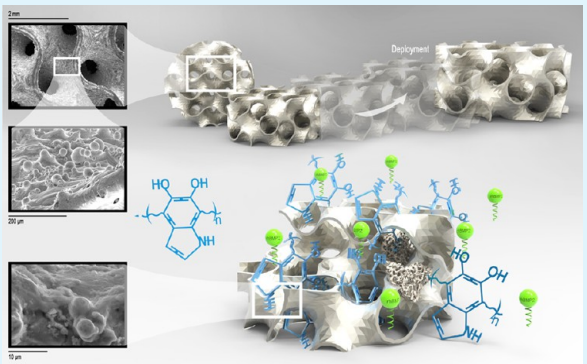

KEYWORDS: *shape memory alloys, additive manufacturing, biomimetic topology, osteogenic coatings, controlled release*

1. INTRODUCTION

Unmet clinical needs in terms of improved implant fixation,[1−3] tissue regeneration,[4−6] infection prevention,[7−9] and complex reconstructive surgeries[10−12] present increasingly more complex challenges that require development of orthopedic biomaterials with multiple advanced functionalities. Traditionally, medical devices received their functionalities either from the bulk material they were made of or from the treatments and coatings applied to their surface. Those two approaches respectively motivated synthesis of new materials for biomedical applications[13−15] and development of surface biofunctionalization techniques.[16−18]

Recent developments in additive manufacturing (AM) techniques not only provide us with a completely new source of functionality, but also make the traditional approaches much more effective. The new source of functionality in AM biomaterials is the arbitrarily complex microarchitectures that could be used to adjust the mechanical properties,[19,20] mass transport properties (e.g., permeability),[21] and tissue regeneration performance.[22−24] Additionally, AM porous biomaterials with complex microarchitectures could be designed with much larger surface areas,[25,26] thereby amplifying the functionalities originating from the surface of biomaterials. In this study, we additively manufactured and surface biofunctionalized porous nitinol to combine the three above-mentioned sources of functionality, namely bulk, surface, and microarchitecture.

In terms of materials, shape memory alloys, such as nitinol, provide extra sources of functionalities originating from the

Received: November 2, 2016
Accepted: December 21, 2016
Published: December 21, 2016

 © 2016 American Chemical Society

DOI: 10.1021/acsami.6b14026
ACS Appl. Mater. Interfaces 2017, 9, 1293−1304

superelastic properties or shape memory effect of material.[27−30] Both above-mentioned properties have been previously used for design of deployable medical devices that could be brought to the site of surgery as minimally invasive as possible.[31,32] The same properties have been also used for fabrication of functional stents.[33,34] Superelastic properties and shape memory behavior of nitinol could, in a similar way, be used for development of deployable orthopedic implants.

As for the surface, polydopamine was used to biofunctionalize the surface of the developed biomaterials through immobilization of rhBMP2. BMP2 has been previously used to improve the bone tissue regeneration performance of biomaterials.[35−38] However, the optimal delivery technique to simultaneously induce the desired osteogenic effects while avoiding the associated side effects is still being intensively researched. Polydopamine has recently emerged[37,39,40] as a promising method for immobilizing rhBMP2 on the surface of orthopedic biomaterials and regulating its release behavior.

Finally, the microarchitecture of the developed biomaterials was rationally designed. Rational design of microarchitecture is the process of choosing the topological properties of the microarchitecture such that a number of design criteria are satisfied. In this study, the design criteria were chosen so as to improve the bone tissue regeneration performance of biomaterials by (1) increasing the surface area of the developed biomaterials and (2) replicating the morphological properties of trabecular bone through the use of minimal surfaces.[41,42] Minimal surfaces are mathematically defined as surfaces that locally minimize their area, and can be shown to possess a mean curvature of zero.[41,42] Minimal surfaces are suggested to improve tissue regeneration performance[43−46] partially due to the similarity between the mean curvature of trabecular bone and that of minimal surfaces.[47,48]

The multiple functionalities of the orthopedic implants that could be developed based on the presented biomaterials therefore include (1) deployability originating from the superelastic behavior, (2) osteogenic behavior stemming from the biofunctionalized surfaces releasing rhBMP2, (3) increased surface area, and (4) surface curvatures similar to those of trabecular bone achieved through the rational design of microarchitecture. We hypothesize that the combination of the above-mentioned design using shape memory nitinol and its manufacturing strategies particularly the surface biofunctionalization process, gives rise to a multifunctional porous biomaterial with significantly improved bone tissue regeneration performance as compared to the as-manufactured biomaterial. The microstructure, mechanical behavior, surface properties, release kinetics, and in vitro cell culture response of the developed biomaterials were extensively studied.

2. MATERIALS AND METHODS

2.1. Rational Design and AM of Porous Biomaterials. Rational design is employed to maximize the bone regeneration performance of AM porous nitinol scaffolds. In this approach, the microarchitecture of the porous nitinol is designed such that a number of preset design criteria are satisfied. The exact design of microarchitecture is then printed using additive manufacturing techniques. In this study, we used the following design criteria: (1) a pore size exceeding 300 μm[49] to enable cell migration and nutrition/oxygenation as well as enhanced tissue regeneration, (2) increased surface area to amplify the effects of surface biofunctionalization, and (3) mean surface curvatures similar to those reported for trabecular bone. To meet the above-mentioned design criteria, we used a specific type of triply periodic minimal surfaces, namely gyroid, as the repeating unit cell based on which the AM porous nitinol was designed. The mean curvature of gyroid type minimal surfaces is zero, which is similar to the mean curvature values observed for trabecular bone.[47,48] Moreover, the design pore size was chosen to be larger than the minimum recommended pore size, that is, 1500 μm (Table 1). Finally, the designed porous structure was calculated to result in two-times larger surface area as compared to a corresponding solid structure (Table 1). The rationally designed specimens (Figure 1) were then additively manufactured via selective laser melting (SLM) technique using a commercial Concept Laser Mlab cusing machine. This machine is equipped with a 100 W continuous (CW) fiber laser with a spot size of 50 μm and a wavelength of 1.06 μm, working under inert argon atmosphere (ensuring an oxygen concentration below 0.6%). The detailed values of manufacturing parameters are presented in Table 2. Prealloyed nitinol powder was provided by AP & C (Raymor, Quebec, Canada) with a particle size range of 25−45 μm. The chemical composition of the powder conformed to the specifications laid out in ASTM F2063 (ASTM International, Standard specification for wrought nickel−titanium shape memory alloys for medical devices and surgical implants) and contained 50.6 at% Ni (according to ICP measurements in a previous work).[50]

Table 1. Rationally Designed and Actual Morphological Properties of Additively Manufactured Porous Nitinol Developed in the Current Study

morphological parameters	design	μCT	geometrical mismatch (%)[a]
open porosity, %	80.0	81.6 ± 2.6	2.0
closed porosity, %	0.00	0.52 ± 0.69	N/A
distance between structure walls, μm	1500	1322 ± 28	−11.9
structure thickness, μm	110	175 ± 32	60.1
surface area, mm^2	393	380 ± 13	−3.3
solid volume fraction, %	9.8	18.4 ± 2.5	87.8

[a]Mismatch percentage is calculated as (μCT − design)/design × 100. N/A, not available.

2.2. Morphological and Biomaterial Characterization. The actual morphological parameters of the porous materials were measured using micro computed tomography (micro-CT). The micro-CT images were obtained with a Phoenix Nanotom S (GE Meausrement and control solutions, Wunstorf, Germany) with a 180 kV/15W high performance nanofocus X-ray tube and a 2304 × 2304 pixel Hamamatsu detector. For scanning in this work, 90 kV and 240 μA with a tungsten target and 0.3 mm copper filter were used. Each sample was scanned over 360° with a 0.15° rotation step with a 500 ms exposure time without any image skip or frame averaging. Image reconstruction was completed using Phoenix datos/x 2.0 reconstruction software (GE Measurement and control solutions, Wunstorf, Germany) and a voxel size of 6.5 μm. CTAn software (Bruker micro-CT. Kontich, Belgium) was applied for 3D morphological analysis of the μCT data. Binarization of the reconstructed μCT images was completed via automatic Otsu segmentation.[51] The same software was then used for determining the actual morphological parameters of the porous structures including open porosity, closed porosity, distance between structural items, structure thickness, surface area, and solid volume fraction. The solid volume fraction of porous structures was calculated by dividing the weight of porous parts by the theoretical weight of the same bounding volume.

The transformation behavior of the laser processed nitinol was analyzed using a TA Instruments Q2000 differential scanning calorimetry (DSC) machine. Heating and cooling cycles were carried out between −130 and 130 °C with a rate of 10 °C/min. The peaks in the heat-flow versus temperature diagram were analyzed to reveal the structure of the SLM nitinol. Further phase analysis of biomaterials was performed using X-ray diffractometry (XRD) to identify the phase constituents of the laser processed nitinol. A Seifert 3003 T/T X-ray diffractometer with Cu−Kα1 radiation and a Theta/2Theta scan type

DOI: 10.1021/acsami.6b14026
ACS Appl. Mater. Interfaces 2017, 9, 1293−1304

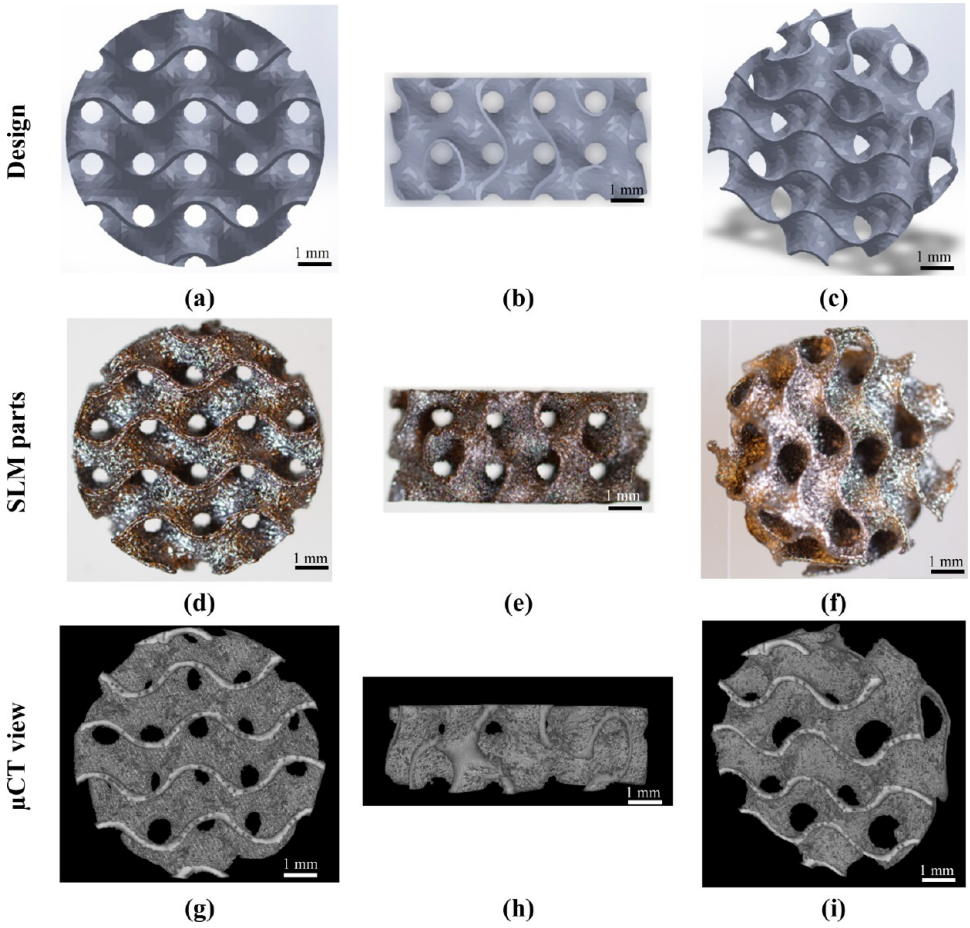

Figure 1. CAD drawings of the porous biomaterials used in the current study from different views (a–c) as well as their corresponding macrographs (d–f) and micro-CT images (g–i) (scale bar: 1 mm).

Table 2. Laser Processing Parameters Used in the Selective Laser Melting Process

laser processing parameters	
laser power, W	30
scanning velocity, mm/s	200
hatch spacing, μm	77
layer thickness, μm	30

operated at 40 kV and 40 mA was used for that purpose. The peaks in the intensity versus 2Theta diffraction were identified and corresponded to the relevant phases.

2.3. Mechanical Testing. The loading–unloading of the laser processed nitinol was performed under compression with strain from 1% to 5% at room temperature using a universal Instron machine. The experiments were repeated three times. The crosshead displacement speed was fixed at 0.1 mm/min. The specimens used for mechanical testing were cylindrical with 11 mm diameter and 11 mm height. Before the compression testing, the surfaces of the specimens were lubricated using zinc stearate to minimize the barreling effects and friction during mechanical testing.

2.4. Surface Biofunctionalization. Four experimental groups were considered in the study including two groups biofunctionalized with low (BL group) and high (BH group) concentrations of immobilized rhBMP2 and two control groups of as-manufactured (AsM group) and polydopamine-coated (DO group) specimens. The as-SLM porous nitinol specimens were biofunctionalized by first anchoring polydopamine (Sigma-Aldrich, Germany) molecules on their surface. The anchored polydopamine molecules were then used for immobilizing rhBMP2 (Sigma-Aldrich, Germany) molecules. The first step of the biofunctionalization process was performed through immersion of the specimens in a 2 mg/mL polydopamine solution, which was prepared by adding polydopamine powder (Sigma-Aldrich, Germany) to 10 mM Tris–HCl buffer (Sigma-Aldrich, Germany) (pH = 8.5) followed by in-dark shaking for 24 h. The second step of the biofunctionalization process was realized by immersing the specimens from the BL and BH groups in solutions of either 100 ng mL^{-1} (BL group) or 500 ng mL^{-1} (BH group) rhBMP2 (Sigma-Aldrich, Germany) in 10 mM Tris-HCl (Sigma-Aldrich, Germany) buffer (pH = 8.5) for 24 h. In the case of the specimens from the DO group, immersion in the polydopamine solution was followed by washing in demineralized water and overnight air drying at room temperature.

The difference between the amount of rhBMP2 in Tris-HCl buffer before and after immersing the specimens was measured using an enzyme-linked immunosorbent assay (ELISA) kit (R&D system, Minneapolis, US) and was assumed to represent the amount of adsorbed (immobilized) rhBMP2. The efficiencies of the immobilization process for the BL and BH specimens were calculated to be respectively 97 ± 0.2% and 96.4 ± 0.4%, corresponding to 47.6 ng and 110 ng of adsorbed rhBMP2 per specimen.

2.5. Surface Characterization. The topographical features and surface morphology of the specimens from various experimental groups were examined using a scanning electron microscope (SEM, JEOL JSM-6500F, Japan). The chemical compositions on the surface of the specimens were determined using both X-ray photoelectron spectroscopy (XPS) and Fourier transform infrared spectroscopy (FTIR). The XPS analysis was performed using an Al Kα X-ray source with 1486.6 eV energy (K-Alpha, Thermo Electron, USA). For characterizing all binding energies, the reference peak was that of the C 1s (at 284.84 eV). The atomic percentage of all elements were

DOI: 10.1021/acsami.6b14026
ACS Appl. Mater. Interfaces 2017, 9, 1293–1304

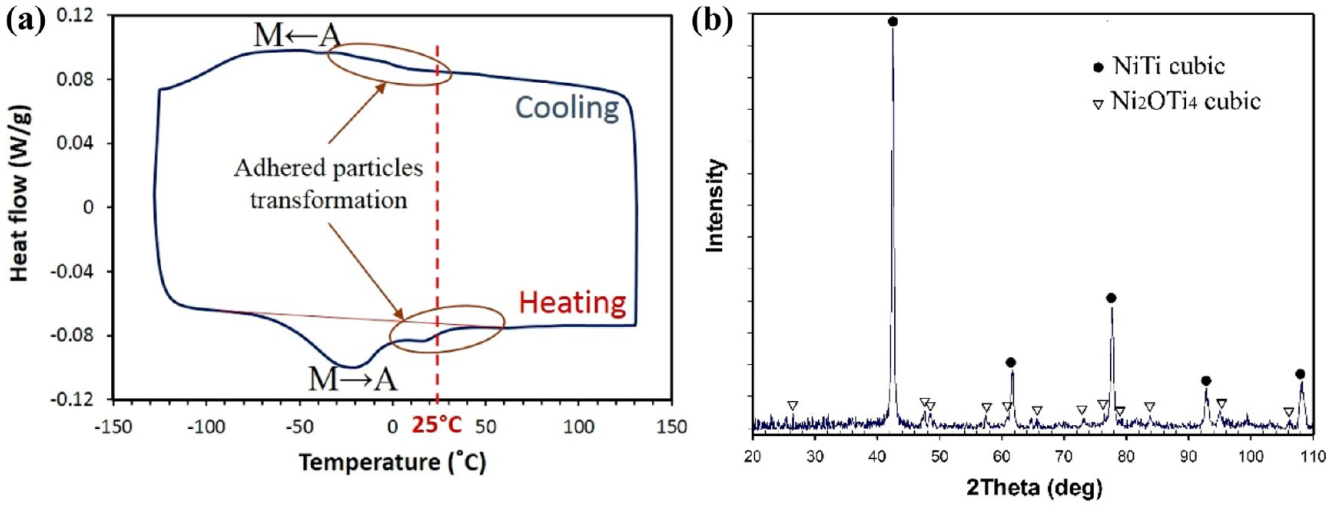

Figure 2. Present phases in SLM-made nitinol porous structures. (a) DSC curves demonstrating the presence of austenite at room temperature and (b) XRD spectrum showing austenite as the main phase along with the presence of oxide constituents such as Ni_2OTi_4.

obtained by normalizing the area of their corresponding peak with respect to the sum of the peaks of all elements.

As for the FTIR analysis, a PerkinElmer Spotlight (Waltham, Massachusetts, US) machine equipped with a mercury cadmium telluride (MCT) detector was employed. The scan parameters were as follows: resolution, 2 1/cm; number of scans per spectrum, 32; wavenumber range, 3200−750 1/cm.

2.6. Release Kinetics and Grafting Content. The kinetic of rhBMP2 release from the specimens of the BL and BH groups was analyzed for up to 28 days (time points: 1, 3, 7, 14, 21, and 28 days) after their incubation in 500 μL of phosphate buffered saline (PBS) maintained at 37 °C. The PBS medium was refreshed after each time point. The concentration of rhBMP2 in the retrieved medium was then measured using an enzyme-linked immunosorbent assay (ELISA) kit (R&D system, Minneapolis, US).

2.7. Cell Viability, Proliferation, and Morphology. Preosteoblast cells from a cell line, namely MC3T3-E1 (ATCC, Germany), were cultured on specimens from various groups with a density of 8×10^4 cells per specimen. The culture medium was α-MEM medium (Invitrogen, US) supplemented with 1% antibiotics (penicillin/streptomycin, Invitrogen, USA), 10% fetal bovine serum (Cambrex, US), and 0.2 mM L-ascorbic acid-2-phosphate (AsAP, Sigma-Aldrich, Germany). The incubation conditions were as follows: 37 °C, 5% CO_2. Live/dead staining was performed at 1 day after culture, for which specimens were incubated for 30 min in fresh wells that contained the staining medium, that is, 2 μM calcein AM and 4 μM ethidium homodimer-1 (Life Technologies, UK). A fluorescence microscope (Olympus BX51, Japan) was employed to observe live (strained green) and dead (stained red) cells.

Cell proliferation was assessed 1, 3, and 7 days after cell culture using the resazurin (Alamar Blue) assay. To prepare the required solution, first a 440 mM solution of resazurin (resazurin sodium salt, Sigma-Aldrich, Germany) in PBS was prepared. The resazurin solution was then diluted to 10% by addition of the α-MEM medium (Invitrogen, US) supplemented with FBS (10%) (Cambrex, US). For each time point, three specimens were transferred to fresh wells containing 600 μL of this solution. A microplate reader (Fluoroskan Ascent FL, Thermo Fisher Scientific, Spain) was employed to measure the absorbance of the medium at 544 nm (with subtraction at 570 nm).

The morphology of the cultured cells after 3 days of culture was observed using a SEM (JEOL JSM-6500F, Japan) at 15 kV. Prior to SEM observation, specimens were immersed in a 2% glutaraldehyde solution followed by serial dehydration in alcohol and drying with hexamethyldisilane (HMDS, Sigma-Aldrich, Germany) to fixate the cells. The specimens were then sputtered with gold (gold layer thickness = 1.7 nm) using a high vacuum film deposition system (Leica EM SCD 500, Germany).

2.8. Alkaline Phosphatase Activity and Calcium Content Assay. Intracellular alkaline phosphatase (ALP) activity was measured at 4, 7, and 14 days after culture using solutions prepared with SIGMAFAST p-nitrophenyl phosphate tablets (Sigma-Aldrich, Germany) as per manufacturer's guidelines. The cells on the specimens were first rinsed with PBS and were subsequently lysed using 0.5% Triton (Triton X-100, Sigma-Aldrich, Germany). The resulting supernatants were then incubated together with 150 μL of the above-mentioned p-nitrophenyl phosphate solution for 30 min. The optical density of the incubation medium was then measured at the 405 nm wavelength (with subtraction at 655 nm) using a microplate reader (VersAmax tunable, Molecular Devices, USA).

The mineralization assay was performed 3 weeks after the start of the culture for which three specimens from each experimental group were moved to fresh wells and rinsed with PBS. The deposited calcium was first extracted through overnight incubation in a 0.6 N HCl solution (room temperature). A calcium kit (Sigma-Aldrich, Germany) was employed to quantify the calcium content. The absorbance of the solution resulting from the calcium kit was measured using a microplate reader (VersAmax tunable, Molecular Devices, USA) at a wavelength of 575 nm.

2.9. Statistical Analysis. The data presented are expressed as mean ± standard deviation (SD) and were analyzed using one-way ANOVA using SPSS (IBM, United States). Data were assumed to be statistically significant different when $p < 0.05$.

3. RESULTS

The actual morphological parameters of the AM porous structures were generally close to the designed parameters, except the structure thickness (and consequently solid volume fraction) built significantly larger than original design (Figure 1, Table 1). This mismatch is a natural outcome of the SLM process, where the used tools (i.e., laser spot diameter and powder size) limits the smallest obtainable geometries. Regardless, micro-CT data confirmed that the actual morphological parameters of the porous structures (e.g., open porosity, good porosity sizes, high surface area, low solid volume fraction, etc.) satisfy the biomimetic design requirements (Table 1, compare with the design criteria).

In terms of metallurgical properties, Figure 2a presents the martensitic transformation behavior (martensite (M) ↔ austenite (A)) of the of SLM nitinol porous structure. As seen, martensitic transformation completes over a large

DOI: 10.1021/acsami.6b14026
ACS Appl. Mater. Interfaces 2017, 9, 1293−1304

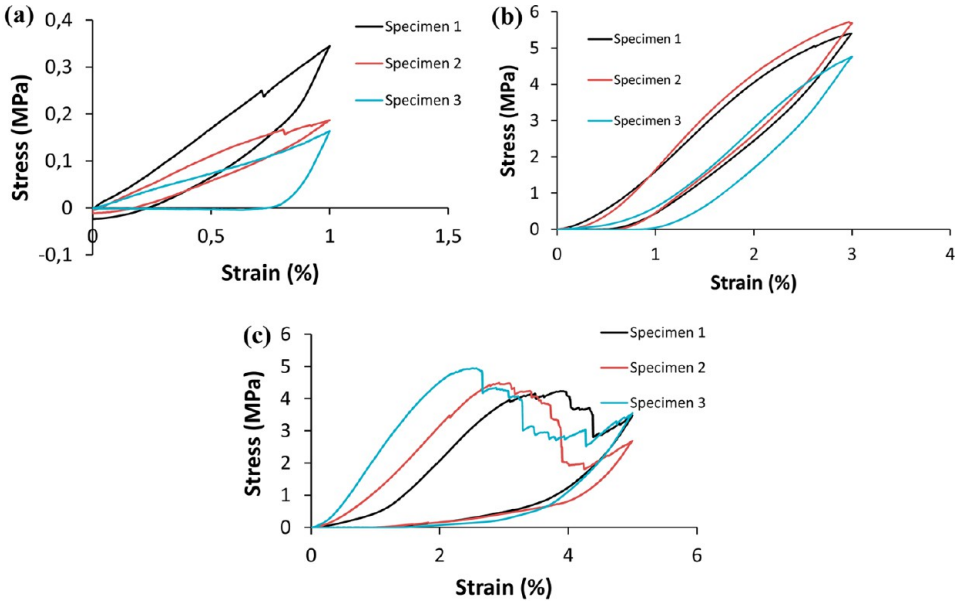

Figure 3. Cyclic compressive stress−strain curves of AM porous biomaterials after (a) 1%, (b) 3%, and (c) 5% strain.

temperature range originating from the adhered particles (i.e., adhered particles to porous structures have different transformation temperature, expanding the DSC curve as an artifact). Nevertheless, transformation completes below room temperature, presenting austenite as the stable phase at 25 °C. This is confirmed by the XRD spectrum (Figure 2b), which exhibits austenitic phase (NiTi cubic) as the main present phase. In addition to austenite, XRD also demonstrates smaller levels of oxides (e.g., Ni_2OTi_4), perhaps originating from large oxide films forming on the extensive surfaces of the used gyroid nitinol porous structure. The presence of the austenite and oxide films will determine the mechanical performance of the products.

The austenite phase in SLM-made nitinol porous structures results in a superelastic behavior at room temperature, as manifested in a full recovery from strains 1% and up to 5% the specimens tested under loading−unloading conditions (Figure 3). This is due to easy twinning deformation of austenite transforming to martensite via loading, while twinned martensite is thermodynamically unstable at room temperature and rapidly transforms back to austenite upon unloading, recovering the implemented strain. The typical stress−strain curves of AM cellular structures, however, include an initial response, a plateau stress, and fluctuating stresses (Figure 4). The initial response before plateau is in fact an artifact originating from the imperfect flatness of unit cells that results in their gradual engagement and loading. After that, transformation of austenite to martensite (via twining mechanisms) enables superelasticity, though the bending deformation might be larger at some unit cells, leading to their early failure. This leads to successive and gradual failure of unit cells leading to the observed fluctuations within the porous structure.

The morphology of the DO specimens showed the presence of a coating with thickness in the range of 5−7 μm as compared to the feature-less surface of AsM specimens (Figure 5a,b). None of the signatures of polydopamine or rhBMP2 was found in the FTIR signal of the specimens from the AsM group (Figure 5c). In contrast, peaks associated with polydopamine[52−55] including N−H bending, N−H shearing, and C═C stretching were observed on the surface of the specimens

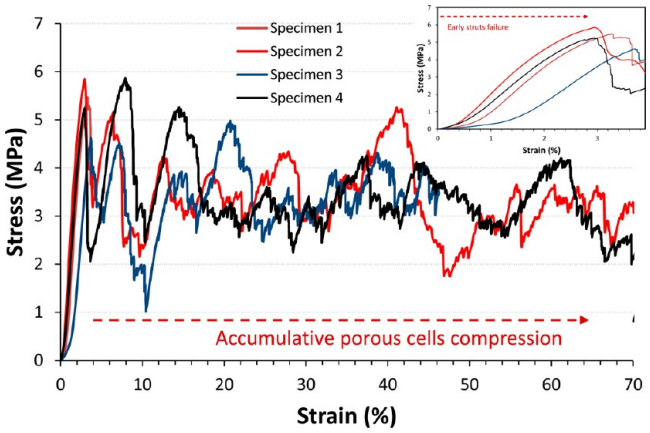

Figure 4. Monotonic (quasi-static) loading curves of AM porous nitinol.

from the other three groups (Figure 5c). Peaks associated with rhBMP2[53,55,56] such as C═O stretching and N−H bending were detected on the surface of the specimens from the BL and BH groups (Figure 5c).

XPS analysis showed the presence of Ni and Ti atoms only on the surface of the AsM specimens and not the specimens from the other groups (Table 3). The atomic percentage of N drastically increased for the specimens from the BH (11.37%), BL (9.37%), and DO (9.15%) groups as compared to those of the AsM group (3.93%) (Table 3). The same holds for C (Table 3). Moreover, N 1s were observed only for the specimens from the DO, BL, and BH groups and not those of the AsM group (Figure 6). The N/C ratio increased from 0.09 for the AsM group to the maximum value of 0.20 for the BH group (Table 3), indicating more than two-fold increase in the N/C value for the BH group. The specimens of the DO and BL groups also showed increased levels of N/C (Table 3). It is known[40] that polydopamine coatings increases the N/C values. The N/C values are known to further increase with immobilization of BMP2 on the surface of biomaterials.[40]

The specimens from both BL and BH group continued to release rhBMP2 up to 28 days after incubation (Figure 7a). The

DOI: 10.1021/acsami.6b14026
ACS Appl. Mater. Interfaces 2017, 9, 1293−1304

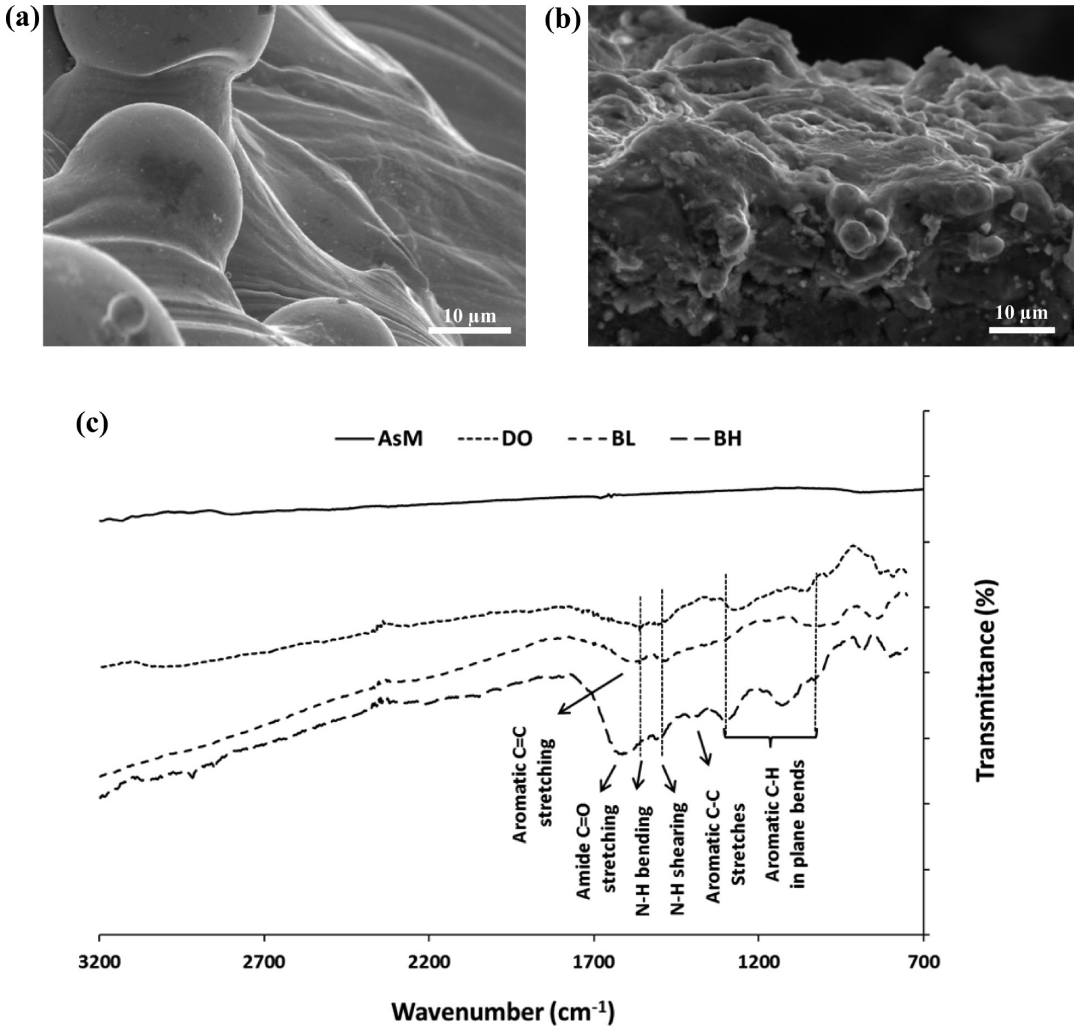

Figure 5. Top surface morphology of the specimens from the (a) AsM and (b) DO groups as well as (c) the FTIR spectra of the specimens from different groups.

Table 3. Chemical Composition Measured on the Surface of Specimens from Different Experimental Groups Using XPS

	atomic percentage (%)					
groups	Ni	Ti	O	C	N	N/C
AsM	5.44	21.42	25.43	43.78	3.93	0.09
DO			23.76	67.09	9.15	0.14
BL			29.91	60.75	9.34	0.15
BH			31.87	56.76	11.37	0.20

difference between the amount of rhBMP2 released from the specimens of the BL and BH groups was very small in the first few days after incubation but gradually increased and reached 12% after 28 days (Figure 7a). After 1 and 3 days, cell numbers as quantified by the Alamar Blue assay were significantly higher for the specimens from the DO, BL, and BH as compared to those of the AsM group (Figure 7b). There was no difference between cell numbers of the various groups after 7 days (Figure 7b). The ALP activity of the specimens from the DO, BL, and BH groups were significantly higher than those of the AsM group after 1, 7, and 14 days of culture (Figure 7c). Moreover, the ALP activity of the specimens from the BH group were also higher than those of the BL and DO groups 14 days after culture (Figure 7b). The calcium content was significantly higher for the BH group as compared to the AsM group (Figure 7d).

No signs of cytotoxicity were observed in the specimens from the DO, BL, and BH group as compared to those of the AsM group (Figure 8). Cells stained red (i.e., red) seemed to appear less frequently in the specimens from the DO, BL, and BH groups as compared to the AsM group (Figure 8), indicating potentially even improvements in cell viability after the biofunctionalization process. Similarly, cell attachment was clearly improved for the specimens from the DO, BL, and particularly BH groups as compared to those of the AsM group (Figure 9). Higher amounts of cells on the specimens from the DO, BL, and BH corresponds with the results of the Alamar Blue assay (Figures 7b and 8). In addition, cells seeded on the specimens from the DO, BL, and BH groups had a healthy spindle-shaped morphology, exhibited more spreading, were organized in several layers, and covered larger parts of the specimen surface as compared to those seeded on specimens from the AsM group (Figure 9). Certain levels of cell bridging (between the surfaces of the porous structure) were observed for the specimens from the BL and BH group that were not present in the specimens from other two groups (Figure 9).

DOI: 10.1021/acsami.6b14026
ACS Appl. Mater. Interfaces 2017, 9, 1293−1304

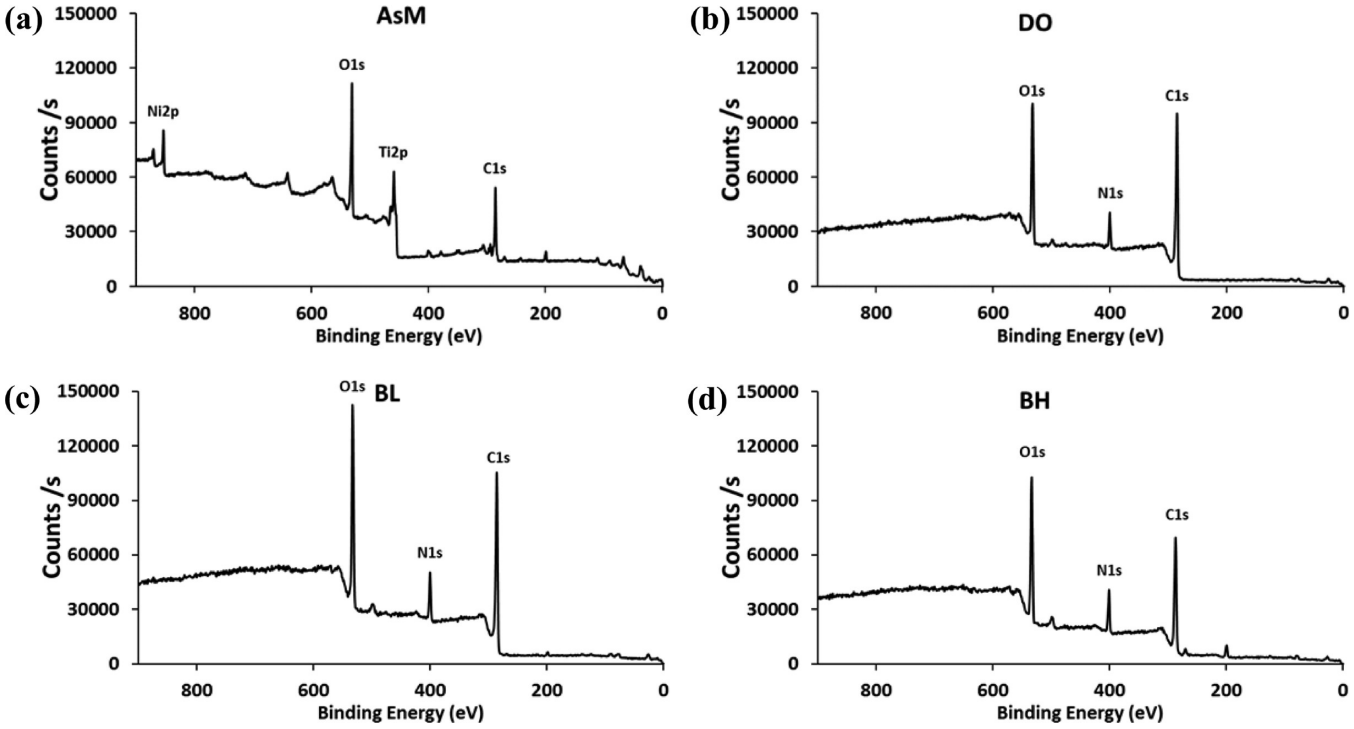

Figure 6. XPS spectra of the specimens from the (a) AsM, (b) DO, (c) BL, and (d) BH groups.

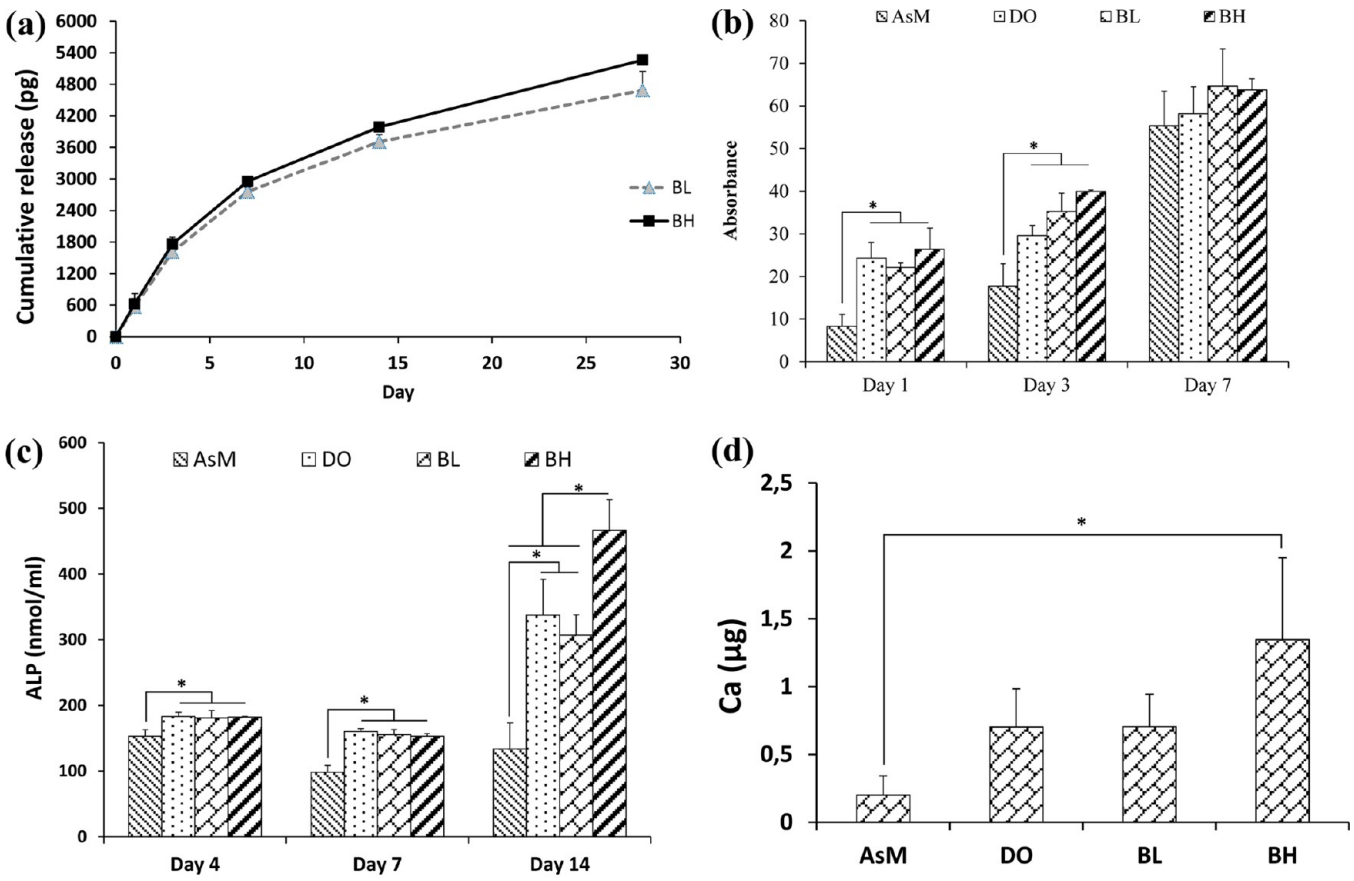

Figure 7. Cumulative release profile of rhBMP2 from (a) BL and BH samples, (b) Alamar Blue absorbance of MC3T3-E1 cells after culturing for 1, 3, and 7 days, (c) ALP activity after incubation for 1, 7, and 14 days, and (d) quantification of mineralized calcium from MC3T3-E1 cultured on different samples for 21 days.

DOI: 10.1021/acsami.6b14026
ACS Appl. Mater. Interfaces 2017, 9, 1293−1304

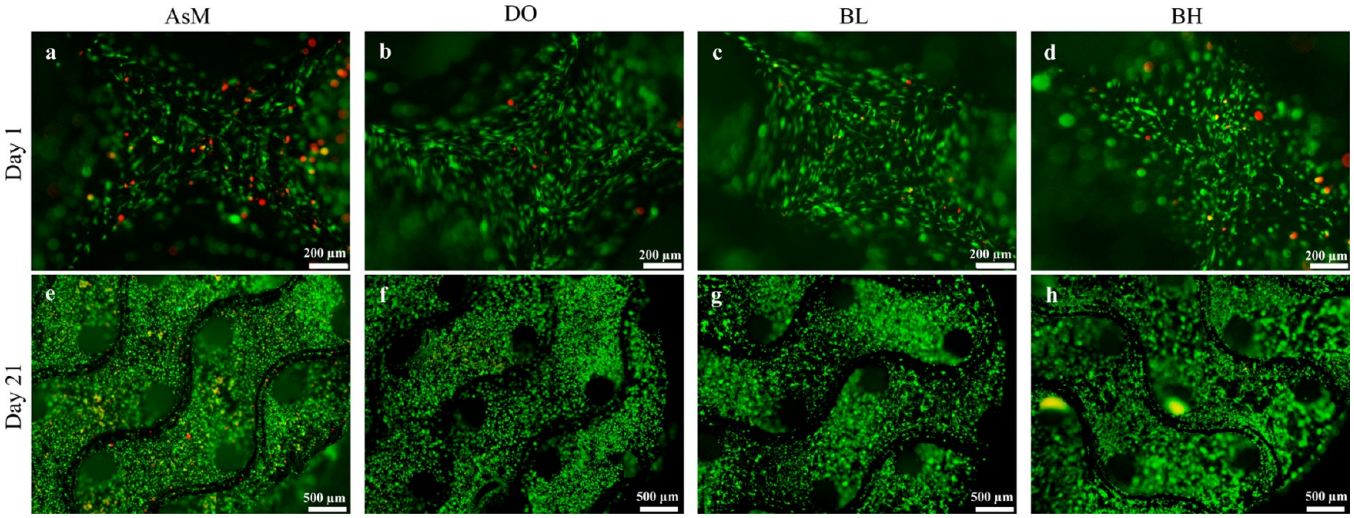

Figure 8. Typical fluorescence images after live/dead staining (green, alive; red, dead) of MC3T3-E1 cells cultured at days 1 and 21 from the (a, e) AsM, (b, f) DO, (c, g) BL, and (d, h) BH specimens.

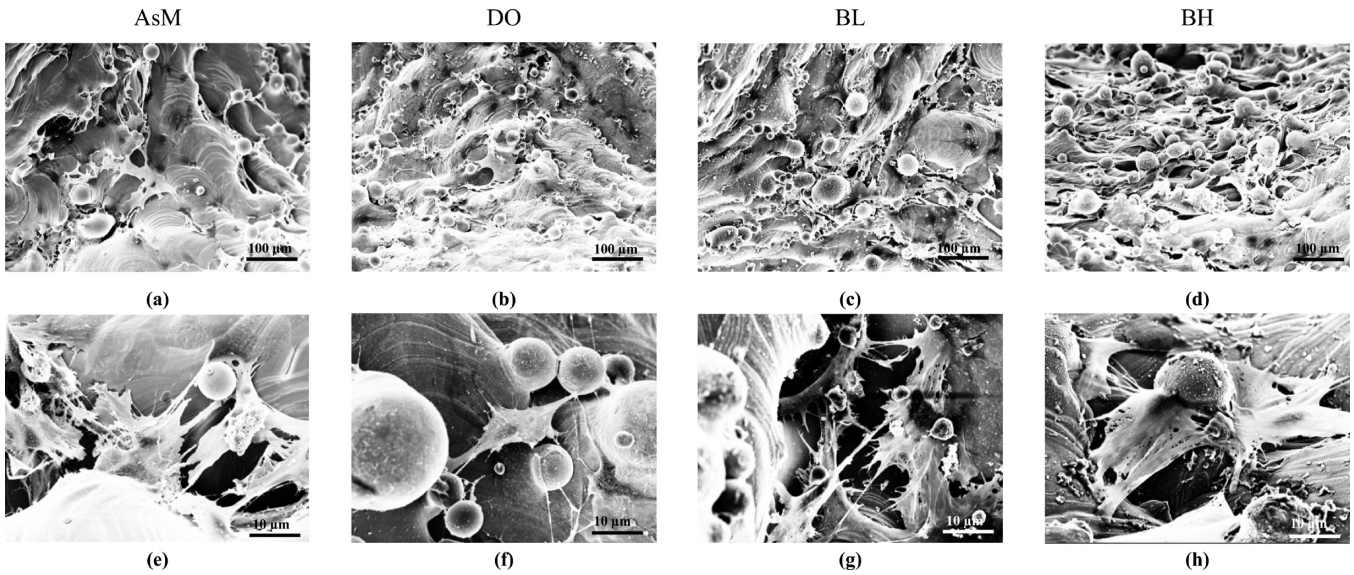

Figure 9. SEM images of the state of cells on the surface of specimens from the (a, e) AsM, (b, f) DO, (c, g) BL, and (d, h) BH groups after incubation for 1 day.

4. DISCUSSION

We aimed to develop AM porous nitinol with multiple functionalities that originate from three distinct sources: properties of the bulk material, the porous microarchitecture, and the biofunctionalized surface. The results clearly show the performance of the developed biomaterial in terms of the different functionalities for which they were rationally designed. The demonstrated superelastic behavior that could be used for development of shape memory and deployable implants is an important example of the functionalities originating from the properties of the bulk material. In terms of microarchitecture, the actual morphological properties of the AM porous biomaterials measured by micro-CT satisfied the rational design requirements in terms of surface curvature, porosity, and pore size. In addition, the rationally designed and AM microarchitecture increased the surface area of the porous biomaterials, as compared to their corresponding solid specimens, thereby amplifying the effects of surface biofunctionalization. Ultimately, the biofunctionalized surfaces resulted in improved cell attachment, cell morphology, and cell proliferation as well as higher levels of ALP activity and calcium content. On the whole, the developed AM porous biomaterials seem to deliver on their promise of combining superelasticity with the benefits of a rationally designed microarchitecture and those of a large and biofunctionalized surface.

4.1. Superelasticity. The AM porous nitinol presented here contained austenite at room temperature (Figure 2), leading to a fully superelastic behavior, being very similar to what is expected from the bone.[57] The superelastic behavior was so ideal that unit cells could regain their original shape even after failure (e.g., see Figure 3b where porous structures regain their original shape after fluctuations in stress−strain curve). This means that the bending-stimulated-failure could not yet generate permanent deformation (via formation of dislocations), allowing a quality bioimplant that will not fail under excessive load (Figure 4) and can regain its primary shape even in the case of partial cell structure failure. It should also be

DOI: 10.1021/acsami.6b14026
ACS Appl. Mater. Interfaces 2017, 9, 1293−1304

noted that the current SLM made porous structure do not provide a very high mechanical strength, perhaps due to the large oxide film forming on the porous surfaces (the oxide layer is extensive enough to be detected by XRD). The oxide layer forms during SLM (due to the presence of 0.6% oxygen during the process), reducing the mechanical performance but increasing the biocompatibility (thicker oxide from laser treated surfaces increase the corrosion resistance and reduces the Ni ion release.[58,59]

Twin-related crystal changes are the main mechanisms to induce reversible martensite to austenite transformation, as a diffusionless transformation through a shear-like mechanism. In the case of superelasticity, when a stress is applied at a specific temperature in which bcc austenite is stable, deformation proceeds until shear-induced martensite is created (if slip does not occur under the applied stress). However, since such martensite is completely unstable at these conditions without the applied loading, the reverse transformation occurs during unloading until the strain completely recovers. This is the case when slip and dislocations do not contribute (when a high critical stress for slip is required while crystal shears are much easier), as such mechanisms induce permanent deformations.[60] The stability of austenite phase originates from two main parallel factors. The first important factor is the chemical composition, for example, oxidation at extensive porous surfaces (to produce products such as Ni_2Ti_4O) reduce the Ti and hence increase the Ni stoichiometric content in the alloy. Ni is an austenitic stabilizer, as above 50 at% efficiently decreases the martensitic transformation temperatures.[61,62] The second factor is the processing parameters such as very high cooling rates originating from the rapid laser movement on small cross sections of the gyroid porous structure in this work. The high cooling rates, in fact, suppress the formation of martensitic stabilizing precipitates (such as Ni-rich Ni_4Ti_3) and reduces the grain sizes. These also contribute to austenite stability.[50,63]

Even though the superelastic behavior of nitinol and other shape memory alloys is not new, AM could add other dimensions to usefulness application of this material property for design and manufacturing of orthopedic implants. Most importantly, superelasticity could be used in the design of deployable implants or implants that could be brought to the surgical site in a compact and be deployed (activated) to change their shape into their final load-bearing/defect-filling shape. The initial compact shape of the implants minimizes the invasiveness of the surgery and could potentially result in shorter operation times and smaller wounds, thereby delivering secondary benefits such as decreased chance of surgery-related complications and implant-associated infections. AM could fulfill two functions in enabling design of more effective deployable implants. First, AM allows for incorporation of complex internal microarchitectures that enable multistability[64−66] and deployability of the implant. Second, the external shape of the deployable implants could be designed to be patient-specific such that, when deployed, it fits the anatomy of the patient. Even though the deployability aspects of AM porous biomaterials were not covered in the current study, the first step has been taken by developing AM porous nitinol with superelastic behavior and complex microarchitectures.

4.2. Microarchitecture and Role of Rational Design. Three criteria were used for rational design of the microarchitecture of biomaterials presented in the current study. The first criterion pertains to the pore size and was chosen to be within the recommended range (to be a good host for the bone cells and simultaneously to allow vascularization), while the increased surface area (as compared to the corresponding solid structure) could enhance the performance of the applied biofunctionalizing coatings.

While understanding the effects of pore size and surface area on tissue regeneration performance of biomaterials is relatively straightforward, the effects of surface curvature are more difficult to understand and were largely neglected until recently. A number of recent studies have shown the importance of surface curvature in tissue regeneration performance of biomaterials.[22−24,67] The tensile stresses developed in cells and their cytoskeleton as a results of their interaction with surfaces are dependent on the surface curvature.[68] Those tensile stresses have been suggested to explain the effects of surface curvature on tissue regeneration performance of biomaterials.[22,24,67,68] Interestingly, geometries that evolve toward minimal surfaces were used in a three-dimensional implementation of a computational model that describes the effects of surface curvature on tissue regeneration.[67] The choice of minimal surfaces with a mean curvature of zero for biomimetic design of the microarchitecture of the porous biomaterials developed here could be further justified by the fact that the mean curvature of trabecular bone is shown to be close to zero.[47,48]

The effects of bone-resembling curvatures, optimal pore sizes, and the two-fold increase in the surface area (resulting in stronger effects of the biofunctionalized surfaces) are reflected in the results of the in vitro cell culture. Both qualitative results in terms of cell invasion and attachment, cell morphology (spreading, healthy spindle shape), surface coverage by cells, and multilayer surface organization and quantitative results in terms of cell proliferation (Alamar Blue assay), ALP activity, and to some extent mineralization clearly show the collective benefits of the three above-mentioned rational design criteria. It is, however, not clear what the contribution of every design criterion is. An extensive study with a formidably large number of specimens in experimental and control groups will enable to systematically separate the effects of different design criteria. However, it is clear that the combination of all applied design criteria results in a strong in vitro performance. In addition, it is suggested that the effects of design parameters such as pore size and pore shape on the performance of the developed biomaterials be considered in the future studies.

4.3. Surface Biofunctionalization. Even though the beneficial effects of BMP2 on bone tissue regeneration performance have been repeatedly demonstrated before, the side effects of BMP2 remain an issue.[69] Optimal delivery of BMP2 is considered an important way for minimizing the side effects of BMP2 while maximizing the tissue regeneration performance of biomaterials. The immobilization of rhBMP2 using polydopamine performed in the current study shows promising results in terms of controlling the release profile of BMP2. First, there is no burst release of all the molecules in the first few days, as immobilization allows for adjusting the release kinetics and enabling active release up to at least 28 days. The second important point is that the immobilization of rhBMP2 using polydopamine allows for regulating the long-term release behavior of independently from the early time release behavior. For example, the release of rhBMP2 from the specimens of the BL and BH groups are almost identical in the first few days and start to deviate from each other in the later time points. That ability to adjust the early time and long-term behaviors

DOI: 10.1021/acsami.6b14026
ACS Appl. Mater. Interfaces 2017, 9, 1293−1304

independently from each other simply by changing the concentration of rhBMP2 in the solution that is used for loading the specimens could have an important function, which is ensuring continuous and long-term stimulation of bone regeneration without causing short-time overdosing and the possible toxic effects associated with that. Indeed, the performance of the specimens from the BL and BH groups as measured by the ALP activity is similar up to 7 days. After 14 days, however, the specimens from the BH group outperform not only specimens from the AsM group, but also those from the BL group. Since the amount of immobilized rhBMP2 in the case of BH specimens (i.e., 110 ng) is about two-times larger than that of BL specimens (i.e., 47.6 ng), this type of dose-dependent difference in the tissue regeneration performance indicators of both groups is expected.

The combination of the above-mentioned functionalities could be used to address the unmet clinical demands in terms of improved implant osseointegration and longevity. In that sense, the biomaterials presented here could be a basis for development of AM[70] patient-specific and deployable implants with rationally designed optimal microarchitectures and adjustable active release mechanisms that are capable of delivering osteogenic molecules and potentially even anti-bacterial agents.

5. CONCLUSIONS

This work aims to combine and assess the in vitro performance of rhBMP2 in relation to nitinol and specific design criteria for improved bone regeneration performance. The microarchitecture of the biomaterials was rationally designed based on triply periodic minimal surface so as to satisfy a number of design criteria. Porous scaffolds were then biofunctionalized using polydopamine-immobilized rhBMP2. The actual morphological properties of the AM porous structures measured by micro-CT closely resembled the design values. DSC revealed austenite phase is stable at room temperature. This was confirmed by XRD that additionally detected significant amount of oxides. XPS and FTIR signals showed the signature peaks of polydopamine and rhBMP2. The release of rhBMP2 continued until 28 days. The early time and long-term rates of release could be adjusted independent of each other simply by changing the concentration of rhBMP2. In vitro cell culture response showed improved cell attachment, cell morphology (spreading, spindle-shaped cell), cell coverage, and cell proliferation as well as enhanced ALP activity and increased calcium content (BH group) for up to 14 days after culture.

AUTHOR INFORMATION

Corresponding Author

*E-mail: s.aminyavari@umcutrecht.nl; saber.aminyavari@gmail.com. Phone: +31-88-7559025.

ORCID

Z. Gorgin Karaji: 0000-0003-2719-7192
M. Speirs: 0000-0002-2377-1671
S. Dadbakhsh: 0000-0003-4120-4790
J.-P. Kruth: 0000-0003-0362-8875
H. Weinans: 0000-0002-2275-6170
A. A. Zadpoor: 0000-0003-3234-2112
S. Amin Yavari: 0000-0003-1677-5751

Notes

The authors declare no competing financial interest.

ACKNOWLEDGMENTS

This work was supported by the Topsector Life Science Health (LSH) program of the Dutch ministry of Education. The support of Eline Kolken for drawing graphical abstract is also acknowledged.

REFERENCES

(1) Maïmoun, L.; Brennan, T. C.; Badoud, I.; Dubois-Ferriere, V.; Rizzoli, R.; Ammann, P. Strontium Ranelate Improves Implant Osseointegration. *Bone* **2010**, *46* (5), 1436−1441.

(2) Mavrogenis, A.; Dimitriou, R.; Parvizi, J.; Babis, G. Biology of Implant Osseointegration. *J. Musculoskelet. Neuronal Interact.* **2009**, *9* (2), 61−71.

(3) Petrie, T. A.; Raynor, J. E.; Reyes, C. D.; Burns, K. L.; Collard, D. M.; García, A. J. The Effect of Integrin-Specific Bioactive Coatings on Tissue Healing and Implant Osseointegration. *Biomaterials* **2008**, *29* (19), 2849−2857.

(4) Arcos, D.; Vallet-Regí, M. Sol−Gel Silica-Based Biomaterials and Bone Tissue Regeneration. *Acta Biomater.* **2010**, *6* (8), 2874−2888.

(5) Hollister, S. J. Porous Scaffold Design for Tissue Engineering. *Nat. Mater.* **2005**, *4* (7), 518−524.

(6) Place, E. S.; Evans, N. D.; Stevens, M. M. Complexity in Biomaterials for Tissue Engineering. *Nat. Mater.* **2009**, *8* (6), 457−470.

(7) Busscher, H. J.; Van Der Mei, H. C.; Subbiahdoss, G.; Jutte, P. C.; Van Den Dungen, J. J.; Zaat, S. A.; Schultz, M. J.; Grainger, D. W. Biomaterial-Associated Infection: Locating the Finish Line in the Race for the Surface. *Sci. Transl. Med.* **2012**, *4* (153), 153rv10−153rv10.

(8) Darouiche, R. O. Treatment of Infections Associated with Surgical Implants. *N. Engl. J. Med.* **2004**, *350* (14), 1422−1429.

(9) Hetrick, E. M.; Schoenfisch, M. H. Reducing Implant-Related Infections: Active Release Strategies. *Chem. Soc. Rev.* **2006**, *35* (9), 780−789.

(10) Marulanda, G. A.; Henderson, E.; Cheong, D.; Letson, G. D. Proximal and Total Humerus Reconstruction with the Use of an Aortograft Mesh. *Clin. Orthop. Relat. Res.* **2010**, *468* (11), 2896−2903.

(11) Scolozzi, P.; Martinez, A.; Jaques, B. Complex Orbito-Fronto-Temporal Reconstruction using Computer-Designed PEEK Implant. *J. Craniofac Surg* **2007**, *18* (1), 224−228.

(12) Wodajo, F. M.; Bickels, J.; Wittig, J.; Malawer, M. Complex Reconstruction in the Management of Extremity Sarcomas. *Curr. Opin. Oncol.* **2003**, *15* (4), 304−312.

(13) Geetha, M.; Singh, A.; Asokamani, R.; Gogia, A. Ti Based Biomaterials, the Ultimate Choice for Orthopaedic Implants−a Review. *Prog. Mater. Sci.* **2009**, *54* (3), 397−425.

(14) Kurtz, S. M.; Devine, J. N. Peek Biomaterials in Trauma, Orthopedic, and Spinal Implants. *Biomaterials* **2007**, *28* (32), 4845−4869.

(15) Staiger, M. P.; Pietak, A. M.; Huadmai, J.; Dias, G. Magnesium and its Alloys as Orthopedic Biomaterials: a Review. *Biomaterials* **2006**, *27* (9), 1728−1734.

(16) Amin Yavari, S.; Ahmadi, S.; van der Stok, J.; Wauthlé, R.; Riemslag, A.; Janssen, M.; Schrooten, J.; Weinans, H.; Zadpoor, A. A. Effects of Bio-Functionalizing Surface Treatments on the Mechanical Behavior of Open Porous Titanium Biomaterials. *J. Mech. Behav. Biomed. Mater.* **2014**, *36*, 109−119.

(17) Chua, P.-H.; Neoh, K.-G.; Kang, E.-T.; Wang, W. Surface Functionalization of Titanium with Hyaluronic Acid/Chitosan Polyelectrolyte Multilayers and RGD for Promoting Osteoblast Functions and Inhibiting Bacterial Adhesion. *Biomaterials* **2008**, *29* (10), 1412−1421.

(18) Shi, Z.; Neoh, K.; Kang, E.; Poh, C. K.; Wang, W. Surface Functionalization of Titanium with Carboxymethyl Chitosan and Immobilized Bone Morphogenetic Protein-2 For Enhanced Osseointegration. *Biomacromolecules* **2009**, *10* (6), 1603−1611.

(19) Ahmadi, S. M.; Yavari, S. A.; Wauthle, R.; Pouran, B.; Schrooten, J.; Weinans, H.; Zadpoor, A. A. Additively Manufactured Open-Cell Porous Biomaterials Made from Six Different Space-Filling Unit Cells:

DOI: 10.1021/acsami.6b14026
ACS Appl. Mater. Interfaces 2017, 9, 1293−1304

the Mechanical and Morphological Properties. *Materials* **2015**, *8* (4), 1871−1896.
(20) Amin Yavari, S.; Ahmadi, S.; Wauthle, R.; Pouran, B.; Schrooten, J.; Weinans, H.; Zadpoor, A. Relationship Between Unit Cell Type And Porosity and the Fatigue Behavior of Selective Laser Melted Meta-Biomaterials. *J. Mech. Behav. Biomed. Mater.* **2015**, *43*, 91−100.
(21) Van Bael, S.; Chai, Y. C.; Truscello, S.; Moesen, M.; Kerckhofs, G.; Van Oosterwyck, H.; Kruth, J.-P.; Schrooten, J. The Effect of Pore Geometry on the In Vitro Biological Behavior of Human Periosteum-Derived Cells Seeded on Selective Laser-Melted Ti6Al4V Bone Scaffolds. *Acta Biomater.* **2012**, *8* (7), 2824−2834.
(22) Bidan, C. M.; Kommareddy, K. P.; Rumpler, M.; Kollmannsberger, P.; Bréchet, Y. J.; Fratzl, P.; Dunlop, J. W. How Linear Tension Converts to Curvature: Geometric Control of Bone Tissue Growth. *PLoS One* **2012**, *7* (5), e36336.
(23) Rumpler, M.; Woesz, A.; Dunlop, J. W.; van Dongen, J. T.; Fratzl, P. The Effect of Geometry on Three-Dimensional Tissue Growth. *J. R. Soc., Interface* **2008**, *5* (27), 1173−1180.
(24) Zadpoor, A. A. Bone Tissue Regeneration: the Role of Scaffold Geometry. *Biomater. Sci.* **2015**, *3* (2), 231−245.
(25) Amin Yavari, S.; Loozen, L.; Paganelli, F. L.; Bakhshandeh, S.; Lietaert, K.; Groot, J. A.; Fluit, A. C.; Boel, C. E.; Alblas, J.; Vogely, H. C.; et al. Antibacterial Behavior of Additively Manufactured Porous Titanium with Nanotubular Surfaces Releasing Silver Ions. *ACS Appl. Mater. Interfaces* **2016**, *8* (27), 17080−17089.
(26) Amin Yavari, S.; Wauthlé, R.; Böttger, A. J.; Schrooten, J.; Weinans, H.; Zadpoor, A. A. Crystal Structure and Nanotopographical Features on the Surface of Heat-Treated and Anodized Porous Titanium Biomaterials Produced Using Selective Laser Melting. *Appl. Surf. Sci.* **2014**, *290*, 287−294.
(27) Dadbakhsh, M. S.; Speirs, M.; Van Humbeeck, J.; Kruth, J.-P. Laser Additive Manufacturing of Bulk and Porous Shape Memory NiTi Alloys: from Processes to Potential Applications. *MRS Bull.* **2016**, *41*, 765−774.
(28) McKelvey, A.; Ritchie, R. Fatigue-Crack Propagation in Nitinol, a Shape-Memory and Superelastic Endovascular Stent Material. *J. Biomed. Mater. Res.* **1999**, *47* (3), 301−308.
(29) McNaney, J. M.; Imbeni, V.; Jung, Y.; Papadopoulos, P.; Ritchie, R. An Experimental Study of the Superelastic Effect in a Shape-Memory Nitinol Alloy under Biaxial Loading. *Mech. Mater.* **2003**, *35* (10), 969−986.
(30) Morgan, E. F.; Bayraktar, H. H.; Keaveny, T. M. Trabecular Bone Modulus−Density Relationships Depend on Anatomic Site. *J. Biomech* **2003**, *36* (7), 897−904.
(31) Duerig, T. W.; Melton, K.; Stöckel, D. *Engineering Aspects of Shape Memory Alloys*; Butterworth-Heinemann, 2013.
(32) Stoeckel, D. Nitinol Medical Devices and Implants. *Minimally invasive therapy & allied technologies* **2000**, *9* (2), 81−88.
(33) Bose, A.; Hartmann, M.; Henkes, H.; Liu, H. M.; Teng, M. M.; Szikora, I.; Berlis, A.; Reul, J.; Simon, C.; Forsting, M.; et al. A Novel, Self-Expanding, Nitinol Stent in Medically Refractory Intracranial Atherosclerotic Stenoses the Wingspan Study. *Stroke* **2007**, *38* (5), 1531−1537.
(34) Stoeckel, D.; Pelton, A.; Duerig, T. Self-Expanding Nitinol Stents: Material and Design Considerations. *Eur. Radiol* **2004**, *14* (2), 292−301.
(35) Bouyer, M.; Guillot, R.; Lavaud, J.; Plettinx, C.; Olivier, C.; Curry, V.; Boutonnat, J.; Coll, J.-L.; Peyrin, F.; Josserand, V.; et al. Surface Delivery of Tunable Doses of Bmp-2 From an Adaptable Polymeric Scaffold Induces Volumetric Bone Regeneration. *Biomaterials* **2016**, *104*, 168−181.
(36) Dadsetan, M.; Guda, T.; Runge, M. B.; Mijares, D.; LeGeros, R. Z.; LeGeros, J. P.; Silliman, D. T.; Lu, L.; Wenke, J. C.; Baer, P. R. B.; et al. Effect of Calcium Phosphate Coating and rhBMP-2 on Bone Regeneration in Rabbit Calvaria Using Poly (Propylene Fumarate) Scaffolds. *Acta Biomater.* **2015**, *18*, 9−20.
(37) Lee, S. J.; Lee, D.; Yoon, T. R.; Kim, H. K.; Jo, H. H.; Park, J. S.; Lee, J. H.; Kim, W. D.; Kwon, I. K.; Park, S. A. Surface Modification of 3D-Printed Porous Scaffolds via Mussel-Inspired Polydopamine and Effective Immobilization of Rhbmp-2 to Promote Osteogenic Differentiation for Bone Tissue Engineering. *Acta Biomater.* **2016**, *40*, 182−191.
(38) Quinlan, E.; Thompson, E. M.; Matsiko, A.; O'Brien, F. J.; López-Noriega, A. Long-Term Controlled Delivery of rhBMP-2 from Collagen−Hydroxyapatite Scaffolds for Superior Bone Tissue Regeneration. *J. Controlled Release* **2015**, *207*, 112−119.
(39) Chien, C.-Y.; Tsai, W.-B. Poly (Dopamine)-Assisted Immobilization of Arg-Gly-Asp Peptides, Hydroxyapatite, and Bone Morphogenic Protein-2 on Titanium to Improve the Osteogenesis of Bone Marrow Stem Cells. *ACS Appl. Mater. Interfaces* **2013**, *5* (15), 6975−6983.
(40) Cho, H.-j.; Madhurakkat Perikamana, S. K.; Lee, J.-h.; Lee, J.; Lee, K.-M.; Shin, C. S.; Shin, H. Effective Immobilization of Bmp-2 Mediated by Polydopamine Coating on Biodegradable Nanofibers for Enhanced In Vivo Bone Formation. *ACS Appl. Mater. Interfaces* **2014**, *6* (14), 11225−11235.
(41) Dierkes, U.; Hildebrandt, S.; Sauvigny, F. *Minimal Surfaces*; Springer, 2010; pp 53−90.
(42) Osserman, R. *A Survey of Minimal Surfaces*; Courier Corporation, 2002.
(43) Kapfer, S. C.; Hyde, S. T.; Mecke, K.; Arns, C. H.; Schröder-Turk, G. E. Minimal Surface Scaffold Designs for Tissue Engineering. *Biomaterials* **2011**, *32* (29), 6875−6882.
(44) Yan, C.; Hao, L.; Hussein, A.; Young, P. Ti−6Al−4V Triply Periodic Minimal Surface Structures for Bone Implants Fabricated via Selective Laser Melting. *J. Mech. Behav. Biomed. Mater.* **2015**, *51*, 61−73.
(45) Yoo, D. Heterogeneous Minimal Surface Porous Scaffold Design Using the Distance Field and Radial Basis Functions. *Med. Eng. Phys.* **2012**, *34* (5), 625−639.
(46) Yoo, D.-J. Computer-Aided Porous Scaffold Design for Tissue Engineering using Triply Periodic Minimal Surfaces. *INT J. PRECIS ENG MAN* **2011**, *12* (1), 61−71.
(47) Jinnai, H.; Nishikawa, Y.; Ito, M.; Smith, S. D.; Agard, D. A.; Spontak, R. J. Topological Similarity of Sponge-Like Bicontinuous Morphologies Differing in Length Scale. *Adv. Mater.* **2002**, *14* (22), 1615−1618.
(48) Jinnai, H.; Watashiba, H.; Kajihara, T.; Nishikawa, Y.; Takahashi, M.; Ito, M. Surface Curvatures of Trabecular Bone Microarchitecture. *Bone* **2002**, *30* (1), 191−194.
(49) Karageorgiou, V.; Kaplan, D. Porosity of 3D Biomaterial Scaffolds and Osteogenesis. *Biomaterials* **2005**, *26* (27), 5474−5491.
(50) Speirs, M.; Wang, X.; Van Baelen, S.; Ahadi, A.; Dadbakhsh, S.; Kruth, J.-P.; Van Humbeeck, J. On the Transformation Behavior of NiTi Shape-Memory Alloy Produced by SLM. *Shape Memory and Superelasticity* **2016**, *2* (4), 310−316.
(51) Kurita, T.; Otsu, N.; Abdelmalek, N. Maximum Likelihood Thresholding based on Population Mixture Models. *Pattern Recognit.* **1992**, *25* (10), 1231−1240.
(52) Jiang, J.-H.; Zhu, L.-P.; Li, X.-L.; Xu, Y.-Y.; Zhu, B.-K. Surface Modification of PE Porous Membranes Based on the Strong Adhesion of Polydopamine and Covalent Immobilization of Heparin. *J. Membr. Sci.* **2010**, *364* (1), 194−202.
(53) Ma, Y.; Zhang, Z.; Liu, Y.; Li, H.; Wang, N.; Liu, W.; Li, W.; Jin, L.; Wang, J.; Chen, S. Nanotubes Functionalized with BMP2 Knuckle Peptide Improve the Osseointegration of Titanium Implants in Rabbits. *J. Biomed. Nanotechnol.* **2015**, *11* (2), 236−244.
(54) Zhu, L.; Lu, Y.; Wang, Y.; Zhang, L.; Wang, W. Preparation and Characterization of Dopamine-Decorated Hydrophilic Carbon Black. *Appl. Surf. Sci.* **2012**, *258* (14), 5387−5393.
(55) Zhu, L.-P.; Jiang, J.-H.; Zhu, B.-K.; Xu, Y.-Y. Immobilization of Bovine Serum Albumin onto Porous Polyethylene Membranes using Strongly Attached Polydopamine as a Spacer. *Colloids Surf., B* **2011**, *86* (1), 111−118.
(56) Renoud, P.; Toury, B.; Benayoun, S.; Attik, G.; Grosgogeat, B. Functionalization of Titanium with Chitosan via Silanation: Evaluation of Biological and Mechanical Performances. *PLoS One* **2012**, *7* (7), e39367.

DOI: 10.1021/acsami.6b14026
ACS Appl. Mater. Interfaces 2017, 9, 1293−1304

(57) Duerig, T.; Pelton, A.; Stöckel, D. An Overview of Nitinol Medical Applications. *Mater. Sci. Eng., A* **1999**, *273-275*, 149−160.
(58) Man, H. C.; Cui, Z. D.; Yue, T. M. Corrosion Properties of Laser Surface Melted NiTi Shape Memory Alloy. *Scr. Mater.* **2001**, *45* (12), 1447−1453.
(59) Muhonen, V.; Heikkinen, R.; Danilov, A.; Jämsä, T.; Tuukkanen, J. The Effect of Oxide Thickness on Osteoblast Attachment and Survival on NiTi Alloy. *J. Mater. Sci.: Mater. Med.* **2007**, *18* (5), 959−967.
(60) Otsuka, K.; Kakeshita, T. Science and Technology of Shape-Memory Alloys: New Developments. *MRS Bull.* **2002**, *27* (02), 91−100.
(61) Frenzel, J.; George, E. P.; Dlouhy, A.; Somsen, C.; Wagner, M.-X.; Eggeler, G. Influence of Ni on Martensitic Phase Transformations in NiTi Shape Memory Alloys. *Acta Mater.* **2010**, *58* (9), 3444−3458.
(62) Lou, J.; He, H.; Li, Y.; Zhu, C.; Chen, Z.; Liu, C. Effects of High O Contents on the Microstructure, Phase-Transformation Behaviour, and Shape-Recovery Properties of Porous NiTi-Based Shape-Memory Alloys. *Mater. Des.* **2016**, *106*, 37−44.
(63) Dadbakhsh, S.; Speirs, M.; Kruth, J. P.; Schrooten, J.; Luyten, J.; Van Humbeeck, J. Effect of SLM Parameters on Transformation Temperatures of Shape Memory Nickel Titanium Parts. *Adv. Eng. Mater.* **2014**, *16* (9), 1140−1146.
(64) Oh, Y. S.; Kota, S. Synthesis of Multistable Equilibrium Compliant Mechanisms Using Combinations of Bistable Mechanisms. *J. MECH DESIGN* **2009**, *131* (2), 021002.
(65) Ohsaki, M.; Nishiwaki, S. Shape Design of Pin-Jointed Multistable Compliant Mechanisms Using Snapthrough Behavior. *STRUCT MULTIDISCIP O* **2005**, *30* (4), 327−334.
(66) Waitukaitis, S.; Menaut, R.; Chen, B. G.-g.; van Hecke, M. Origami Multistability: from Single Vertices to Metasheets. *Phys. Rev. Lett.* **2015**, *114* (5), 055503.
(67) Bidan, C. M.; Wang, F. M.; Dunlop, J. W. A Three-Dimensional Model for Tissue Deposition on Complex Surfaces. *Comput. Methods Biomech Biomed Engin* **2013**, *16* (10), 1056−1070.
(68) Gamsjäger, E.; Bidan, C.; Fischer, F.; Fratzl, P.; Dunlop, J. Modelling the Role of Surface Stress on the Kinetics of Tissue Growth in Confined Geometries. *Acta Biomater.* **2013**, *9* (3), 5531−5543.
(69) James, A. W.; LaChaud, G.; Shen, J.; Asatrian, G.; Nguyen, V.; Zhang, X.; Ting, K.; Soo, C. A Review of the Clinical Side Effects of Bone Morphogenetic Protein-2. *Tissue Eng., Part B* **2016**, *22* (4), 284−297.
(70) Zadpoor, A. A.; Malda, J. Additive Manufacturing of Biomaterials, Tissues, and Organs. *Ann. Biomed. Eng.* **2016**, 1−11.

DOI: 10.1021/acsami.6b14026
ACS Appl. Mater. Interfaces 2017, 9, 1293−1304